

Journal of Materials Chemistry A

Accepted Manuscript



This is an *Accepted Manuscript*, which has been through the Royal Society of Chemistry peer review process and has been accepted for publication.

Accepted Manuscripts are published online shortly after acceptance, before technical editing, formatting and proof reading. Using this free service, authors can make their results available to the community, in citable form, before we publish the edited article. We will replace this *Accepted Manuscript* with the edited and formatted *Advance Article* as soon as it is available.

You can find more information about *Accepted Manuscripts* in the [Information for Authors](#).

Please note that technical editing may introduce minor changes to the text and/or graphics, which may alter content. The journal's standard [Terms & Conditions](#) and the [Ethical guidelines](#) still apply. In no event shall the Royal Society of Chemistry be held responsible for any errors or omissions in this *Accepted Manuscript* or any consequences arising from the use of any information it contains.

Cite this: DOI: 10.1039/c0xx00000x

www.rsc.org/xxxxxx

ARTICLE TYPE

Architectural design and phase engineering of N/B-codoped TiO₂(B)/anatase nanotube assemblies for high-rate and long-life lithium storage

Chaoji Chen,^a Xianluo Hu,^{*a} Bao Zhang,^b Ling Miao^b and Yunhui Huang^{*a}⁵ Received (in XXX, XXX) Xth XXXXXXXXXX 20XX, Accepted Xth XXXXXXXXXX 20XX

DOI: 10.1039/b000000x

TiO₂ polymorphs hold great promise as anode candidates in lithium-ion batteries (LIBs) because of their low cost, enhanced safety and high power capability, but they suffer from poor electrical conductivity and low lithium-ion mobility. Herein, an attractive nanoassembly made of ultrathin TiO₂ nanotubes with
10 selected phases and hetero-atom doping was developed through a mild ionothermal reaction. The grain interface of TiO₂(B)/anatase, N/B codoping, and nanoassembly were elaborately engineered. They offer effective nanohighways for fast electronic and Li-ion transport, when applied as an anode in LIBs. The carbon-free, N/B-codoped TiO₂(B)/anatase nanotube nanoassemblies exhibit exceptionally high rate capability and good durability (160 mA h g⁻¹ at 12 A g⁻¹ and retaining 140 mA h g⁻¹ even after 500
15 cycles). This work demonstrates that the integrated design of surface states and electronic structures plays a crucial role in exploring new capabilities of TiO₂ polymorphs for electrochemical energy storage.

Introduction

Large-scale renewable energy storage techniques require low cost,
20 high safety, long cycle life and desired energy and power output.^{1,2} Among them, lithium-ion batteries (LIBs) represent one of the most promising techniques because of their high energy density and environmental friendliness.^{3,4} Nevertheless, LIBs with a commercial anode of graphite is difficult to meet these
25 requirements. For instance, the formation of lithium dendrites and the solid electrolyte interphase (SEI) causes the safety issues, especially at high charge/discharge rates.^{5,6} Owing to enhanced safety and lifetime, Ti-based anode materials with the operating potential (1.5–1.8 V versus Li/Li⁺) and the specific capacity
30 (170–330 mA h g⁻¹) have aroused much attention. In principle, Ti-based electrodes operate within the electrochemical stability window of the electrolyte solution, in which the severe generation of SEI and lithium plating could be avoided. Spinel Li₄Ti₅O₁₂ is a well-established anode material that can deliver outstanding
35 performances at high charge/discharge rates.^{7–10} However, the low specific capacity (175 mA h g⁻¹) hinders its practical application, which has driven scientists to explore the electrochemical properties of alternative Ti-based materials such as TiO₂ polymorphs.

40 Theoretically, TiO₂ can store one Li⁺ ion per formula unit with a similar potential range and a higher specific capacity of 335 mA h g⁻¹ (nearly a twofold increase over the capacity of Li₄Ti₅O₁₂).^{11–22} Among the TiO₂ polymorphs, the monoclinic TiO₂(B) is an exception that can deliver enhanced power
45 capability and bulk capacity.^{23,24} Intriguingly, the crystal structure

of TiO₂(B) features channels that are parallel to the *b* and *c*-axes.²⁵ This unique open-channel framework may offer both active sites and diffusion paths for Li⁺ ions. Meanwhile, the enhanced performance of TiO₂(B) benefits from its fast
50 pseudocapacitive (de-)insertion behavior, rather than the slow solid-state diffusion-controlled lithium storage in the typical intercalation materials. Despite these advantages, however, the poor electronic conductivity together with metastability of TiO₂(B) is still the main limitation. Several strategies have been
55 proposed to address this issue. For example, aliovalent doping, incorporating TiO₂ with carbon nanotubes/graphene and carbon coating, have been proven to be viable routes to improve the electronic conductivity of TiO₂.^{26–33} However, aliovalent doping requires complicated procedures or high-temperature sintering,
60 and therefore metastable TiO₂(B) can hardly be maintained in the final product. It should also be noted that irreversible capacity loss may occur due to the irreversible Li-ion trapping in the carbon layer or other conductive matrix. Also, the carbonaceous additives (e.g., amorphous carbon, carbon nanotubes, and
65 graphene) often contribute to the negligible capacity within the operating potential window for TiO₂ (normally higher than 1.0 V vs. Li/Li⁺). Nanostructuring has been the most widely used strategy to enhance the Li-ion mobility, whereby higher Li-ion insertion/extraction kinetics is achieved by reducing the length of
70 Li-ion pathways.^{17,34–36} However, low tap densities and stringent protocols of fine nanopowders not only impact the production cost but also limit the practical applications. To meet the ever increasing demand for safe and high-rate electrode materials, an

integrated design by elaborately tailoring the crystal phase, surface, and electronic structure of TiO₂ nanomaterials without using carbon additives is of great significance but a significant challenge.

Here, we report the design and fabrication of unique nanoassemblies constructed of TiO₂(B)/anatase thin nanotubes with tailored local grain interface and electronic structure through a mild ionothermal route. These TiO₂(B)/anatase nanotubes are ~10 nm in outer diameter and ~3 nm in wall thickness. Benefiting from the synergistic effects of N/B codoping, TiO₂(B)/anatase grain boundary, and architectural assembly, effective nanohighways for fast electronic transport and Li-ion mobility could be realized in the TiO₂-based electrodes, enabling a remarkable high rate capability and good durability. A reversible capacity as high as 160 mA h g⁻¹ is successfully achieved at a current density of 12 A g⁻¹ with a high initial Coulombic efficiency of 94.8%, and 140 mA h g⁻¹ is maintained even after 500 cycles with Coulombic efficiencies of nearly 100%. The cyclic voltammetry (CV) and galvanostatic charge-discharge analysis demonstrate the abundant grain interfaces of TiO₂(B)/anatase mixed phases promote additional interfacial lithium storage. First-principle calculations based on the density of states suggest that the engineering of the electronic structures is beneficial to both Li-ion diffusion and electronic transport. Our approach does not involve carbonaceous hybridization as well as post surface coating by carbon or conductive polymers, and it is potentially competitive for scaling-up production. Most importantly, this work not only provides high-performance electrodes for next-generation energy storage applications, but offer ideal candidates for elucidating the underlying insights into superior electrochemical high-rate and cycling behaviors of TiO₂.

Experimental

Materials Synthesis

For the preparation of N/B-codoped TiO₂(B)/anatase nanotube assemblies, 3 g of metatitanic acid (TiO₂·H₂O) of industrial grade was added into 40 mL of NaOH solution (10 M) under stirring for 10 min, and 4 mL of [Bmim][BF₄] ionic liquid was injected under vigorously stirring for 20 min. Then, the mixture was transferred into a 75-mL Teflon-coated autoclave and heated at 200 °C for 30 h. The precipitate was collected by centrifugation, washed with DI water, exchanged with H⁺ (using a solution of 0.1 M HCl), and then washed again with DI water until the pH value reaches 7. The obtained precursor was dried at 60 °C for 24 h, and then thermally treated at 350 °C for 4 h in air. If the heating temperature was increased to 500 °C, the assembled anatase nanorods were obtained. For comparison, TiO₂(B) nanobelts were also prepared under the same condition for the product of the N/B-codoped TiO₂(B)/anatase nanotube assemblies, except that the [Bmim][BF₄] ionic liquid was not used.

Materials Characterization

The morphology and structure of the products were determined by scanning electron microscopy (SEM, SIRION200), transmission electron microscopy (TEM, JEOL JEM-2010F), X-ray diffraction (XRD, PANalytical B.V., Holland), and X-ray photoelectron spectroscopy (XPS, VG MultiLab 2000 system

with a monochromatic Al K α X-ray source, Thermo VG Scientific). Raman spectra were collected on a Renishaw Invia spectrometer with an Ar⁺ laser of 514.5 nm at room temperature.

Electrochemical measurements

The electrochemical properties were investigated in 2032 coin cells, whereby the working electrodes were prepared by a slurry made of active material, super P, and binder (polyvinylidene fluoride dissolved in N-methyl-2-pyrrolidone solvent) in 8:1:1 by weight. The Cu foil was used as the current collector. The lithium foil worked as the counter and reference electrodes, Celgard 2300 as the separator, and 1 M LiPF₆ dissolved in ethylene carbonate and dimethyl carbonate (1:1 by volume) as the electrolyte. Cyclic voltammetry and electrochemical impedance spectra (EIS) over the frequency range of 100 kHz to 0.01 Hz were collected on a PARSTAT 2273 potentiostat. Galvanostatic charge/discharge measurements were performed on a Land Battery Measurement System (Land, China) at different current densities within a potential window of 3–1 V at room temperature.

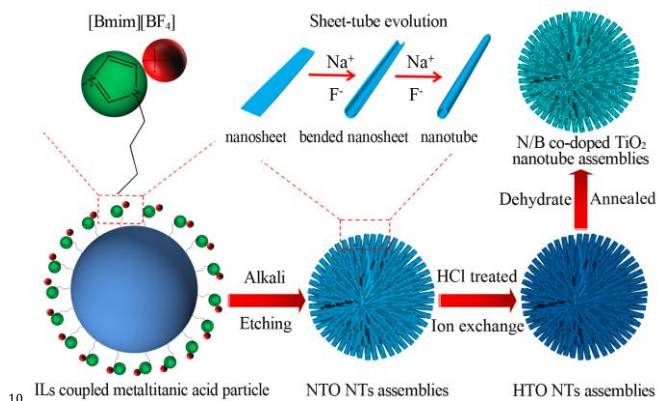
DFT Calculation

The first-principle calculations are performed based on density functional theory (DFT) implemented in the VASP³⁷ package, and the electronic states were expanded using the projector augmented wave (PAW)³⁸ approach with a cutoff of 400 eV. The exchange-correlation energy is described by the functional of Perdew-Burke-Ernzerhof (PBE)³⁹ based on general gradient approximation (GGA). A 1 × 3 × 2 supercell of 144 atoms is calculated to model N/B-doped bulk TiO₂ (B). The Brillouin zone is sampled with 4 × 4 × 4 Monkhorst mesh⁴⁰, and the force convergence thresholds are 0.02 eV/Å.

Results and discussion

The nanoassemblies constructed of TiO₂ nanotubes were synthesized through the ionothermal process of metatitanic acid (TiO₂·H₂O) in a concentrated NaOH solution in the presence of an appropriate amount of [Bmim][BF₄] ionic liquid (IL), followed by H⁺ ion exchange and thermal treatment. The formation process of the TiO₂ nanotubes during the ionothermal process may follow the growth mechanism of “nanosheet scrolling”.⁴¹ This could be further confirmed by our time-dependent experiments and morphology evolution of the products (Fig. S1). Scheme 1 illustrates the whole process for the formation of the assembled TiO₂ nanotubes. Firstly, the IL-coupled TiO₂·H₂O precursor dispersed in the condensed NaOH solution will transform into sheet-like lamellar structures. Then, the asymmetrical chemical environment arising from the imbalance of Na⁺/H⁺/F⁻ ion concentrations near both sides of each nanosheet would give rise to excess surface energy and force the nanosheet to scroll into nanotube (Fig. S2). Na⁺ ions between the interlayer of the as-formed titanate could be exchanged easily by smaller H⁺ ions via dilute HCl treatment. Further thermal treatment facilitates the removal of H⁺ and O²⁻ ions in the form of H₂O and the rearrangement of TiO₆ octahedra, leading to the formation of monoclinic TiO₂(B) or/and anatase TiO₂. Since titanate and TiO₂(B)/anatase possess the common structural features containing TiO₆ octahedra and zigzag ribbons

in the crystal lattices, both of them may inherit the tubular morphology from the titanate precursor during the mild thermal treatment (350 °C for 4 h). If the heating temperature is increased to 500 °C, the TiO₂(B)/anatase nanotubes evolved into solid rods of anatase TiO₂ (Fig. S3a-d). Also, control experiments indicate that [Bmim][BF₄] plays a crucial role in the morphology of the products. TiO₂(B) nanobelts were obtained by a traditional hydrothermal process without using any [Bmim][BF₄] (Fig. S3e-h).



Scheme 1 Schematic illustration for the formation process of the N/B-co-doped TiO₂ nanotube assemblies through a mild ionothermal route (NTO: Na₂Ti₃O₇; HTO: H₂Ti₃O₇; NTs: nanotubes).

The crystalline structure of the product was characterized by XRD. Fig. 1a displays a typical XRD pattern for the product obtained by ionothermal synthesis with a subsequent thermal treatment at 350 °C for 4 h. This pattern can be indexed to the monoclinic phase of TiO₂(B) (JCPDF no. 74-1940), together with a minor phase of anatase (JCPDF 21-1272). Representative SEM images of the assembled TiO₂ nanotubes are shown in Fig. 1b and 1c. Evidently, the spherical assemblies are made of a large number of nanotubes. Closer observations by TEM indicate that individual nanotube has an outer diameter of ~10 nm and a wall thickness of ~3 nm, as shown in Fig. 1d and 1e. Interestingly, the packing density of those assembled TiO₂ nanotubes is much higher than that of single TiO₂(B) nanobelts obtained by a traditional hydrothermal reaction at the absence of [Bmim][BF₄] with a subsequent treatment at 350 °C for 4 h (Fig. S4). This is assigned to the secondary architecture featuring dense aggregates of nanotubes. It is expected that the coupled advantages of higher packing density and thin walls would endow the TiO₂ nanotubes with higher specific volumetric capacity and faster charge/discharge for LIB applications. The high-resolution TEM (HRTEM) image (Fig. 1f) and the selected-area electron diffraction (SAED) pattern (Fig. 1g) further confirm the mixed crystal phases of TiO₂(B) and anatase. The grain interfaces between TiO₂(B) and anatase could be identified in the HRTEM image. Further analysis reveals that the interface generates from the matching of the TiO₂(B) (002) plane and the anatase (101)

plane with an angle of 65°. Fig. 1h schematically illustrates the grain interface between anatase and TiO₂(B).

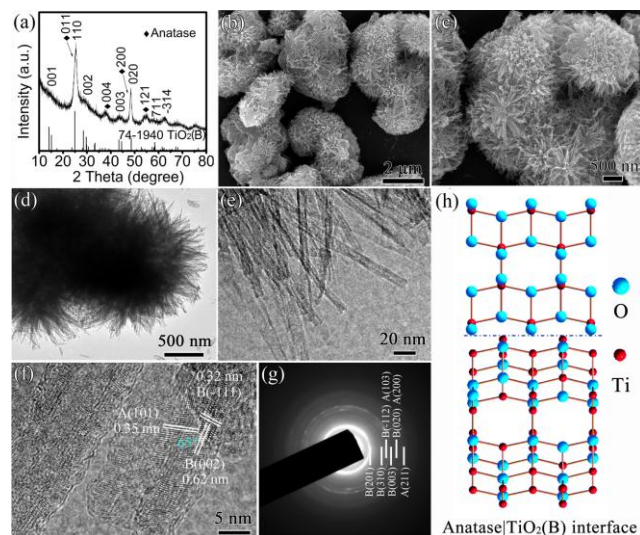


Fig. 1 (a) XRD pattern, (b,c) SEM images, (d,e) TEM images, (f) HRTEM image, and (g) SAED pattern for the as-formed TiO₂ nanotube assemblies. (h) Illustration of the grain interface between anatase and TiO₂(B).

Raman spectroscopy provides a nondestructive technique to determine the quality of crystals or amorphous compounds. The exact phase compositions of the TiO₂ products obtained under different conditions were further quantified by Raman spectroscopy in combination with calculations based on the areas of the fitted peaks.⁴² Based on the areas of the fitted peaks at 144 cm⁻¹ for anatase and 123 cm⁻¹ for TiO₂(B), the mass ratio for the anatase phase can be quantified according to the relation: $\chi_A = I_A / \{I_A + I_B\} * [6.2 - 5.2 I_A / (I_A + I_B)]$, where χ_A presents the proportion of anatase phase, I_A and I_B are the normalized areas of the fitted peaks at 144 and 123 cm⁻¹, respectively. Calculation results suggest the existence of TiO₂(B) are quantified to be ~100 wt.% for nanobelts, ~81% for assembled nanotubes, and ~2% for assembled nanorods, respectively (Fig. 2a-c).

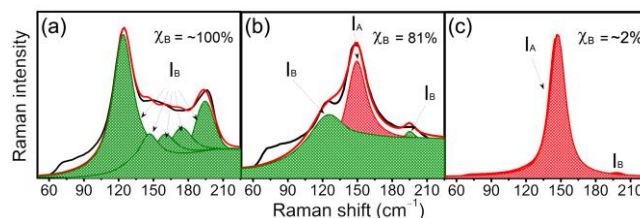


Fig. 2 The fitted peaks of the Raman spectra for the products of (a) TiO₂(B) nanobelts, (b) TiO₂ nanotube assemblies, and (c) TiO₂ nanorod assemblies. χ_B is the mass proportion of the TiO₂(B) phase in the products.

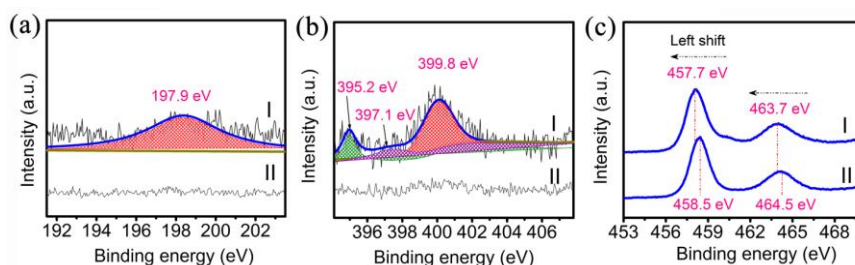


Fig. 3 High-resolution XPS spectra for the TiO₂ nanotube assemblies (I) and the TiO₂(B) nanobelts (II): (a) B 1s; (b) N 1s; and (c) Ti 2p.

XPS measurements were further performed to gain insight into the surface electronic structure and the chemical valent of the products, as shown in Fig. 3. In addition to Ti and O elements, the XPS spectra show that the B and N elements do not exist in the TiO₂ nanobelts, but in the assembled TiO₂ nanotubes obtained at the presence of [Bmim][BF₄]. The dopant contents of B and N are about 1.0 at% and 1.15 at%, respectively. It is believed that the N and B elements originate from the starting reactant of [Bmim][BF₄]. To determine the electronic states of the dopants, high-resolution XPS spectra of Ti 2p, B 1s, and N 1s were investigated. The B 1s peak at 197.9 eV in the product of assembled TiO₂ nanotubes is assigned to the Ti–B bond of the TiO₂ lattice (Fig. 3a).⁴³ It is known that the N 1s peak at 395.2 eV is characteristic of N atoms in the O–Ti–N sites substitutionally incorporated into the TiO₂ lattice. The N 1s peaks at 395–397 eV assigned to the Ti–N bonding in N-doped TiO₂ have also been reported by other groups.^{44–46} Another N 1s peak at ~399.8 eV is associated with the Ti–O–N bonding (Fig. 3b). The N atoms substitutionally or/and interstitially located in the TiO₂ lattice, as summarized by Fujishima and co-workers⁴⁷, can be determined

by the N 1s peak locations (~400 eV for the interstitial N dopant and ~396 eV for the substitutional N dopant). The XPS spectra of B 1s and N 1s reveal that the B atoms may be substitutionally doped into the TiO₂ lattice whereas the N atoms both substitutionally and interstitially locate in the TiO₂ lattice. As the electronegativity of N and B atoms is larger than that of Ti atoms, a doped B or N atom will attract an O atom in the TiO₂ lattice, thus prompting the formation of oxygen atom vacancies and the reduction of Ti⁴⁺ into Ti³⁺.^{43,48} This conclusion was further supported by the XPS spectra of Ti 2p (Fig. 3c). The binding energies of 458.5 eV for Ti 2p_{3/2} and 464.5 eV for Ti 2p_{1/2} are observed in un-doped TiO₂ nanobelts. In contrast, the binding energies of 457.7 and 463.7 eV for the N/B-codoped TiO₂ nanotubes are 0.8 eV lower, due to the existence of Ti³⁺ ions.^{10,43,48} Moreover, it is found that the TiO₂ nanorods obtained by thermal treatment at 500 °C only contain the N dopant rather than the B dopant (Fig. S5).

The lithium-storage performance of the TiO₂ products was evaluated using lithium half-cells. Fig. 4a demonstrates the rate performance for the electrode made of assembled N/B-codoped

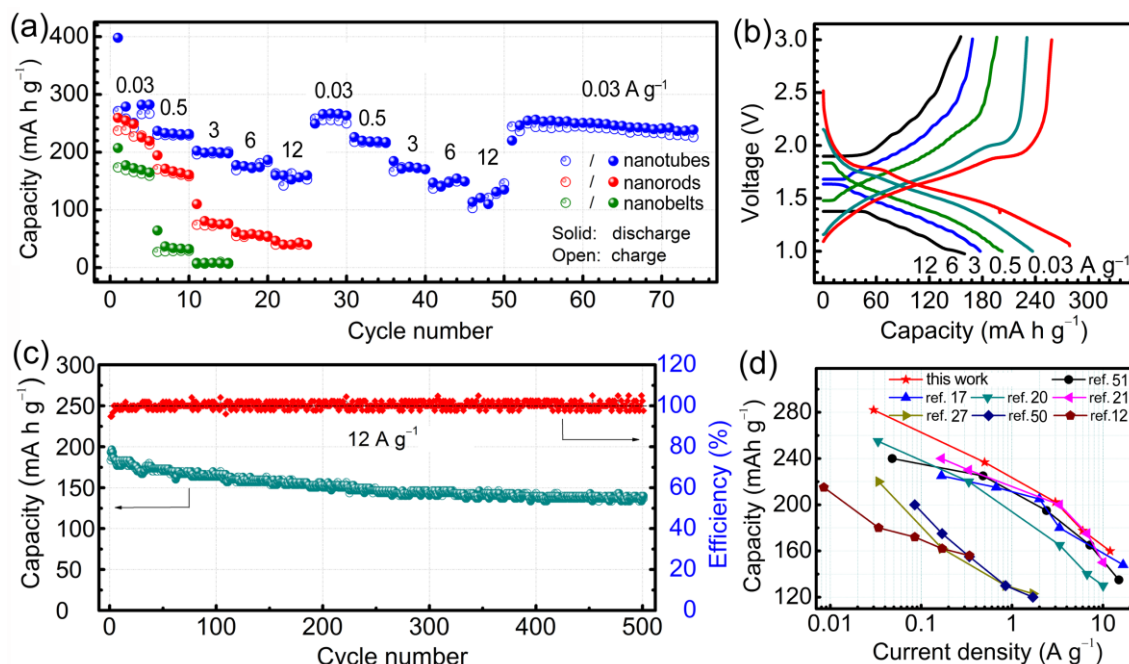


Fig. 4 (a) Rate performances of the TiO₂ nanotube assemblies, TiO₂ nanorods and TiO₂(B) nanobelts. (b) Discharge-charge curves of the TiO₂ nanotube assemblies at different current densities of 0.03, 0.5, 3, 6, and 12 A g⁻¹. (c) Cycling performance of the TiO₂ nanotube assemblies. (d) Comparison of the rate performances between the present TiO₂ nanotube assemblies and the previous reports on the TiO₂-based electrodes.^{12,17,20,21,27,50,51}

TiO₂ nanotubes at various C rates. Reversible discharge capacities of 279, 237, 202, and 178 mA h g⁻¹ can be achieved at 0.03, 0.5, 3 and 6 A g⁻¹, respectively. Impressively, a capacity of 160 mA h g⁻¹ with a high initial Coulombic efficiency of 94.8% (retaining 67.5% of the capacity at 0.5 A g⁻¹) can still be gained at a superhigh charging-discharging rate of 12 A g⁻¹, representing the superior rate performances ever achieved for TiO₂-based materials.^{11–15,17–22,26–32,49–52} The capacities towards current densities of the assembled TiO₂ nanotubes and previously reported TiO₂ electrodes plotted on the Ragone diagram (Fig. 4d) directly demonstrate the superior rate capability of the assembled TiO₂ nanotubes in this work. The charge-discharge profiles at various C rates show similar shapes despite the slightly aggravation of polarization as the current densities increase, indicating the excellent structure stability even through extremely fast Li⁺ insertion/extraction (Fig. 4b). Fig. 4c shows the cycling performance of the electrode made of assembled TiO₂ nanotubes at a high rate of 12 A g⁻¹, with a retained capacity of ~140 mA h g⁻¹ even after 500 cycles and Coulombic efficiencies of nearly 100%, suggesting the excellent cyclability of this electrode. For comparison, the electrodes made of TiO₂ nanobelts and nanorods obtained in this work were also evaluated under the similar measurement conditions. However, they deliver much lower capacities than that of assembled TiO₂ nanotubes, especially at high rates (Fig. 4a).

The fundamental understanding on the underlying structure-performance relationship is of great importance to achieve high-performance electrodes for LIBs. In this work, cyclic voltammetry and galvanostatic charge-discharge profiles have been obtained to identify the capacity contribution from different lithium storage processes. Fig. 5a–c displays the representative CV curves for the electrodes made of TiO₂ nanobelts, nanotubes, and nanorods, respectively within the potential window of 1.0–3.0 V at a scan rate of 0.2 mV s⁻¹. Clearly, the shape of these profiles is quite different from each other, suggesting the characteristic electrochemical behaviors associated with different

TiO₂ crystal phases. For the electrode made of the pure TiO₂(B) nanobelts, a pair of cathodic/anodic peaks at ~1.4/1.65 V (S peaks) are observed in the CV curve (Fig. 5a), which is assigned to the lithium insertion into TiO₂(B). However, the cathodic peak gradually shifted to the lower potential during the subsequent cycles, mainly as a result of the aggravating polarization of the TiO₂(B) nanobelts due to the low intrinsic conductivity. Fig. 5b shows the CV curves for the electrode made of the N/B-codoped TiO₂ nanotube assemblies. In addition to two pairs of S-peaks, a pair of A-peaks at ~1.75/1.90 V can be observed^{13,20,21,53}, and the shape could be well maintained after 5 cycles, even at higher scan rate of 1 and 2 mV s⁻¹ (Fig. S6). The S and A-peaks suggest not only the pseudocapacitive Li-cycling behaviour in TiO₂(B) but also the solid-state Li-diffusion in anatase. For the electrode made of the anatase TiO₂ nanorods (Fig. 5c), only a pair of A-peaks were observed. Among these TiO₂-based electrode, it is noted that the CV curves for the TiO₂ nanotube assemblies exhibit the largest enclosed area, indicating the high-capacity accommodation of Li⁺ ions in the N/B-codoped TiO₂(B)/anatase nanotubes. Fig. 5d–f shows the galvanostatic charge-discharge curves for the three TiO₂-based electrodes. The discharge curves could be divided into three or four regions in light of the distinct slopes at each region, subject to different lithium storage processes in the electrodes. In this case, the four regions represent the solid-solution Li⁺ insertion (OCV → 1.75 V), solid-state diffusion of Li⁺ in anatase (plateau at 1.75 V), pseudocapacitive lithium storage in TiO₂(B) (1.75 → ~1.4 V), and interfacial lithium storage (~1.4 → ~1.0 V), respectively. Correspondingly, the capacity contribution from the four regions is summarized as histograms for the three TiO₂-based electrodes in Fig. 5g–i. It is not a surprise that the capacity contribution from Region II is absent for the nanobelts (Fig. 5g), due to the pure phase of TiO₂(B). It is observed that the main capacity contribution for the TiO₂(B) nanobelts is from Region III (140 mA h g⁻¹) together with a low capacity of 30 mA h g⁻¹ from Region I and 40 mA h g⁻¹ from Region IV. For the TiO₂(B)/anatase nanotubes, the

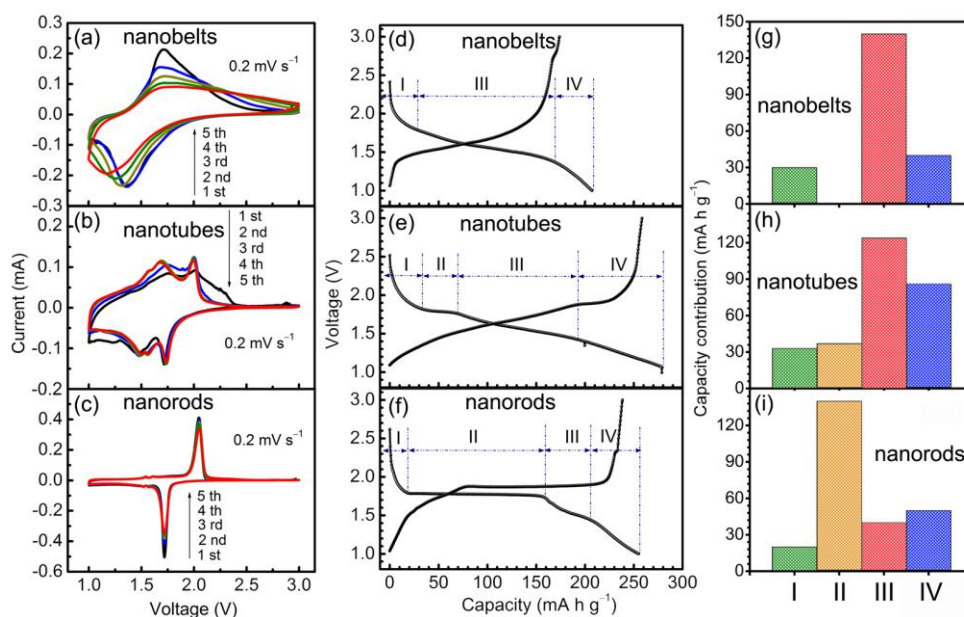


Fig. 5 (a,b,c) CV curves at a scan rate of 0.2 mV s⁻¹, (d,e,f) Charge-discharge voltage profiles at 30 mA g⁻¹, and (g,h,i) Capacity contribution from the different regions (I-IV) of discharge curves in d–f for the three products of TiO₂(B) nanobelts, TiO₂ nanotube assemblies and anatase TiO₂ nanorods.

capacities of 33 mA h g⁻¹ from Region I, 37 mA h g⁻¹ from Region II, 124 mA h g⁻¹ from Region III, and 86 mA h g⁻¹ from Region IV can be achieved, contributing to a total capacity of 280 mA h g⁻¹. For the anatase TiO₂ nanorods, the major capacity of 140 mA h g⁻¹ is from Region II, and a long plateau appears at 1.75 V, characteristic of lithium insertion into the anatase host. From the detailed distribution of the capacity contribution for the three TiO₂-based electrodes (Fig. S7), the following conclusions can be drawn: 1) the difference between Region I (solid-solution Li⁺ insertion) is negligible, namely, almost structure-independent; 2) the capacity contribution from Region II and III is highly phase-dependent; 3) the TiO₂(B)/anatase nanotube assemblies deliver the largest capacity contribution related to the interfacial lithium storage (Region IV). As proposed by Jamnik and Maier⁵⁴, the interfaces in a battery system can provide active sites for additional Li-ion storage. In particular, Li-ion storage in the grain interface with a Li⁺-accepting phase and an electron-accepting phase may happen through a "Job-sharing" process.⁵⁴ In the case of mixed TiO₂ phases, this "Job-sharing" phenomenon is prone to occur with respect to the fact that holes tend to move towards the TiO₂(B) phase, electrons to the anatase phase in the grain interface. Recently, Wu *et al.*¹³ also demonstrate that the grain boundaries in the anatase spheres decorated with a small amount of TiO₂(B) nanodots are proposed to store Li⁺ ions via this "Job-sharing" or "charge separation" mechanism. In our work, it is believed that the grain interfaces between anatase and TiO₂(B) may also offer active sites for Li-ion storage.

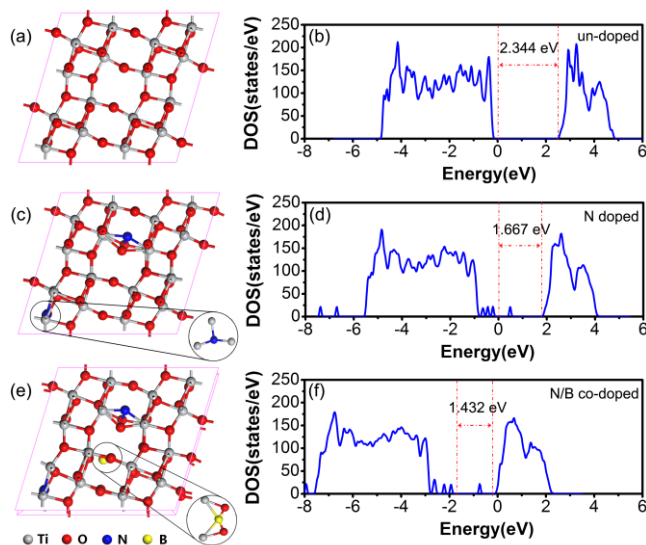


Fig. 6 (a) Relaxed structures of pristine TiO₂(B), (c) substitutional and interstitial N doped TiO₂(B), and (e) substitutional and interstitial N/substitutional B codoped TiO₂(B). Density of states: (b) pristine, (d) N-doped, and (f) N/B-codoped TiO₂(B).

Furthermore, we have carried out first-principle calculations to simulate the density of states (DOSs) of the doped and undoped products. N can site in the lattice of TiO₂ interstitially or substitutionally while B locates in TiO₂ substitutionally. The substitutional S_N4 and interstitial I_N2 sites for N and the substitutional S_B4 site for B doping were determined based on the energy calculations (Fig. S8 and Table S1, more calculation

details presented in the supplementary method). Fig. 6a–f shows the relaxed structures and the corresponding DOSs of the undoped, N-doped, and N/B-codoped TiO₂. In the N-doped model, the dopants introduce some impurity levels that broaden the valence band, thus reducing the band gap of TiO₂ and improving the electronic conductivity. For the N/B-codoped TiO₂, a similar reduced band gap is found. Furthermore, the Fermi level in the N/B-codoped TiO₂ is positioned within the conduction band, and the electron concentration in the conduction band is improved, thus leading to enhanced electronic conductivity of the N/B-codoped TiO₂. The synergic effects of N/B codoping in enhancing the electronic conductivity may contribute to the superior high-rate capability of the electrode made of N/B-codoped TiO₂(B)/anatase nanotube assemblies.

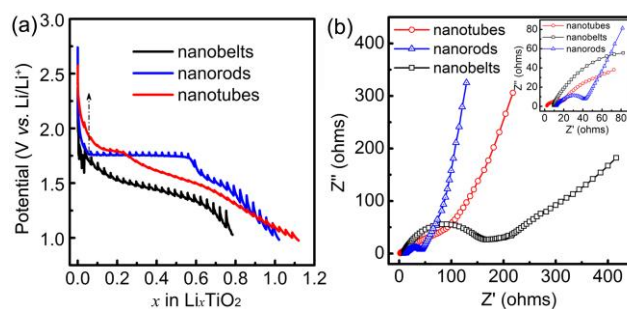
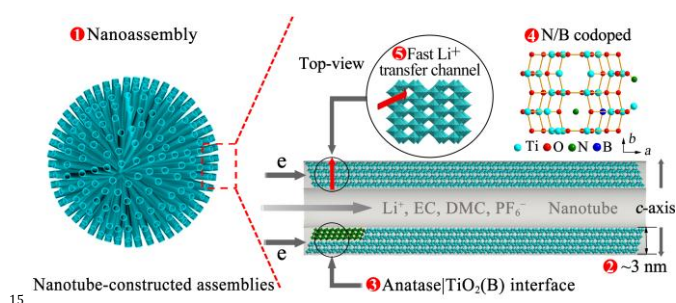


Fig. 7 (a) Voltage composition profiles obtained via the GITT technique during discharge and (b) AC impedance spectra for the three products of TiO₂(B) nanobelts, TiO₂ nanotube assemblies, and TiO₂ nanorods.

The Li-ion mobility in bulk TiO₂ is also very crucial to the electrochemical performance. The galvanostatic intermittent titration technique (GITT) as well as electrochemical impedance spectra has been performed to explore the influence of ionic conductivity. GITT curves in Fig. 7a demonstrate the evolution of the quasi-equilibrium voltage for the three samples. It is worth noting that the distribution of the potential before the plateau increases as the particle size of the products decreases. In principle, smaller particles possess shorter surface-to-core distances and more surface active sites, and lower energy barrier is involved. The Nyquist plots in Fig. 7b show that the diameter of the semicircle in the high-medium frequency region for the electrode made of TiO₂ nanotube assemblies is much smaller than those of the electrodes made of anatase nanorods and TiO₂(B) nanobelts, suggesting a smallest charge-transfer resistance (R_{ct}) in the electrode of the nanotube assemblies. Meanwhile, the Z'-intercept assigned to the electrode-electrolyte interface resistance (R_e) for the electrode made of the nanotube assemblies is also the smallest. This indicates the good contact between the active material and the electrolyte, probably due to the assembly of TiO₂ nanotubes into advanced secondary architectures on a micrometer scale. The sloped tails in the low-frequency region is ascribed to the Li-ion diffusion process, or the so-called Warburg diffusion (Z_w). Previous studies reveal that the Li-ion diffusion coefficient (D_{Li}) can be quantified according to the relation: $D_{Li} = 0.5[V_m * (-dE/dx)/(FA\delta)]^{55}$, where V_m is the molar volume of the compound, A is the surface area of the electrode, F is the Faraday constant, δ is the Warburg factor calculated from the relation of $Z' = \delta\omega^{-1/2}$, and dE/dx can be calculated from the GITT curves.

Calculations according to the above relations reveal that the Li-ion diffusion coefficient in the N/B-codoped TiO₂(B)/anatase nanotube assemblies is higher than those of the TiO₂(B) nanobelts and the anatase nanorods (Detailed data are listed in Table S2). A recent study by Wagemaker³⁴ and co-workers reveals that the grain boundary in nanosized TiO₂ promotes the fast transport of Li⁺ ions, since the barrier of the nucleation and interstitial phase boundary movement is pretty low. Thus, the faster lithiation process is achieved, compared with the solid-state Li-ion diffusion in microsized TiO₂. Besides, the existence of Ti³⁺ ions is beneficial to the interstitial Li-ion diffusion. As a result, the coupled advantages of grain boundary and nanostructuring would contribute to a higher D_{Li} in the assembled TiO₂(B)/anatase nanotubes.



Scheme 2 Graphical illustration of the structural factors (1–5) towards the electrochemical behaviour of lithium ions in the TiO₂ nanotube assemblies/electrolyte system.

Scheme 2 graphically illustrates the synergistic effects of nanoassembly, domain size, grain interface, dopants and crystal structure that contribute to the lithium storage performance (thus the rate capability) in the TiO₂(B)/anatase nanotubes/Li cell containing the electrolyte of LiPF₆ dissolved in ethylene carbonate (EC) and dimethyl carbonate (DMC). The nanoassemblies with micrometer-sized scales offer a high packing density and fine process ability for manufacturing electrodes. Meanwhile, the reduced domain size (~3 nm) would shorten the transport distance of Li⁺ ions, giving rise to quicker response of Li⁺ ions in the active material. It is also proven that the bending of tubular structures with structural distortions would promote lithium storage.^{17,23} The ultrathin walls of the TiO₂ nanotubes combined with the distorted tubular structure should partially account for the enhanced electrochemical performance. Furthermore, the grain interfaces of anatase|TiO₂(B) along with the interstitial N dopant offer abundant sites for additional lithium storage. This interfacial lithium storage behavior driven by the grain interface has a faster kinetic than the solid-state diffusion, benefiting the high rate capability. Meanwhile, the N/B codoping would facilitate the fast transport of both electrons and Li⁺ ions, thus enhancing the electronic and ionic conductivities simultaneously. Considering the main phase of TiO₂(B) in the nanotube assemblies, the unique open framework and low-energy Li-ion pathway undoubtedly help to improve the rate capability.

Conclusions

In summary, we have successfully synthesized unique N/B-codoped TiO₂(B)/anatase nanotube assemblies by a reproducible

mild ionothermal method. The as-prepared TiO₂ serves as an anode materials for LIBs, and delivers a high rate capability of 160 mA h g⁻¹ at a current density of 12 A g⁻¹ with a high initial Coulombic efficiency of 94.8%. The high performance is related to the effective “nanohighways” that allow fast electronic transport and Li-ion diffusion, benefiting from the unique configuration of ultrathin-nanotube assemblies with a higher packing density, the coupled crystallographic structures of TiO₂(B)/anatase offering grain boundaries and enhanced ionic conductivity, and the N/B-codoping enhancing electronic conductivity. Most importantly, our high-performance TiO₂-based materials without carbon additives operate within the electrochemically stable window of the electrolyte solution. Moreover, the phase-, morphology-, and composition-dependent performances are studied in detail, which helps shed light on the underlying Li-cycling mechanisms of TiO₂ polymorphs. This work opens up an opportunity to consider these materials for high-power and safe LIB applications or other fields of low-cost large-scale energy storage.

Acknowledgments

This work was supported by National High-tech R&D Program of China (863 Program, No. 2015AA034601) and National Natural Science Foundation of China (No. 51522205, 51472098 and 21271078).

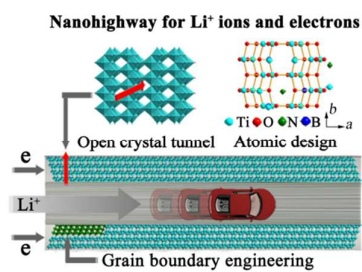
Notes and references

- ^a State Key Laboratory of Materials Processing and Die & Mould Technology, School of Materials Science and Engineering, Huazhong University of Science and Technology, Wuhan 430074, China
- ^b Wuhan National Laboratory for Optoelectronics, and School of Optical and Electronic Information, Huazhong University of Science and Technology, Wuhan 430074, P. R. China
E-mail: huxl@mail.hust.edu.cn (X.L. Hu)
- B. Dunn, H. Kamath and J. M. Tarascon, *Science*, 2011, **334**, 928-935.
 - J. Liu, J. G. Zhang, Z. G. Yang, J. P. Lemmon, C. Imhoff, G. L. Graff, L. Y. Li, J. Z. Hu, C. M. Wang, J. Xiao, G. Xia, V. V. Viswanathan, S. Baskaran, V. Sprenkle, X. L. Li, Y. Y. Shao and B. Schwenzer, *Adv. Funct. Mater.*, 2013, **23**, 929-946.
 - M. Armand and J. M. Tarascon, *Nature*, 2008, **451**, 652-657.
 - J. B. Goodenough and K. S. Park, *J. Am. Chem. Soc.*, 2013, **135**, 1167-1176.
 - N. Takami, A. Satoh, M. Hara and T. Ohsaki, *J. Electrochem. Soc.*, 1995, **142**, 371-379.
 - D. Aurbach, E. Zinigrad, Y. Cohen and H. Teller, *Solid State Ionics*, 2002, **148**, 405-416.
 - J. H. Liu, J. S. Chen, X. F. Wei, X. W. Lou and X. W. Liu, *Adv. Mater.*, 2011, **23**, 998-1002.

8. L. F. Shen, B. Ding, P. Nie, G. Z. Cao and X. G. Zhang, *Adv. Energy Mater.*, 2013, **3**, 1484–1489.
9. H. H. Xu, X. L. Hu, Y. M. Sun, W. Luo, C. J. Chen, Y. Liu and Y. H. Huang, *Nano Energy*, 2014, **10**, 163-171.
10. L. F. Shen, E. Uchaker, X. G. Zhang and G. Z. Cao, *Adv. Mater.*, 2012, **24**, 6502-6506.
11. M. Sondergaard, K. J. Dalgaard, E. D. Bojesen, K. Wonsyld, S. Dahl and B. B. Iversen, *J. Mater. Chem. A*, 2015, DOI: 10.1039/C5TA04110D.
12. J. F. Ye, W. Liu, J. G. Cai, S. Chen, X. W. Zhao, H. H. Zhou and L. M. Qi, *J. Am. Chem. Soc.*, 2010, **133**, 933-940.
13. Q. L. Wu, J. G. Xu, X. F. Yang, F. Q. Lu, S. M. He, J. L. Yang, H. J. Fan and M. M. Wu, *Adv. Energy Mater.*, 2015, **5**, 1401756.
14. G. Q. Zhang, H. B. Wu, T. Song, U. Paik and X. W. Lou, *Angew. Chem. Int. Ed.*, 2014, **53**, 12590-12593.
15. B. Wang, Y. Bai, Z. Xing, D. Hulicova-Jurcakova and L. Z. Wang, *ChemNanoMat*, 2015, **1**, 96-101.
16. G. Jeong, J.-G. Kim, M.-S. Park, M. Seo, S. M. Hwang, Y.-U. Kim, Y.-J. Kim, J. H. Kim and S. X. Dou, *ACS Nano*, 2014, **8**, 2977-2985.
17. Y. Ren, Z. Liu, F. Pourpoint, A. R. Armstrong, C. P. Grey and P. G. Bruce, *Angew. Chem. Int. Ed.*, 2012, **51**, 2164-2167.
18. S. H. Liu, Z. Y. Wang, C. Yu, H. B. Wu, G. Wang, Q. Dong, J. S. Qiu, A. Eychmüller and X. W. Lou, *Adv. Mater.*, 2013, **25**, 3462-3467.
19. Y. X. Tang, Y. Y. Zhang, J. Y. Deng, J. Q. Wei, H. L. Tam, B. K. Chandran, Z. L. Dong, Z. Chen and X. D. Chen, *Adv. Mater.*, 2014, **26**, 6111-6118.
20. H. S. Liu, Z. H. Bi, X. G. Sun, R. R. Unocic, M. P. Paranthaman, S. Dai and G. M. Brown, *Adv. Mater.*, 2011, **23**, 3450-3454.
21. S. H. Liu, H. P. Jia, L. Han, J. L. Wang, P. F. Gao, D. D. Xu, J. Yang and S. N. Che, *Adv. Mater.*, 2012, **24**, 3201-3204.
22. H. Hu, L. Yu, X. H. Gao, Z. Lin and X. W. Lou, *Energy Environ. Sci.*, 2015, **8**, 1480-1483.
23. A. G. Dylla, G. Henkelman and K. J. Stevenson, *Acc. Chem. Res.*, 2013, **46**, 1104-1112.
24. Z. Liu, Y. G. Andreev, A. Robert Armstrong, S. Brutti, Y. Ren and P. G. Bruce, *Prog. Nat. Sci.-Mater.*, 2013, **23**, 235-244.
25. C. J. Chen, Y. W. Wen, X. L. Hu, X. L. Ji, M. Y. Yan, L. Q. Mai, P. Hu, B. Shan and Y. H. Huang, *Nat. Commun.*, 2015, **6**, 6929.
26. Y. Qiao, X. L. Hu, Y. Liu, C. J. Chen, H. H. Xu, D. F. Hou, P. Hu and Y. H. Huang, *J. Mater. Chem. A*, 2013, **1**, 10375-10381.
27. S. J. Ding, J. S. Chen, D. Y. Luan, F. Y. C. Boey, S. Madhavi and X. W. Lou, *Chem. Commun.*, 2011, **47**, 5780-5782.
28. C. J. Chen, X. L. Hu, Z. H. Wang, X. Q. Xiong, P. Hu, Y. Liu and Y. H. Huang, *Carbon*, 2014, **69**, 302-310.
29. C. J. Chen, X. L. Hu, Y. Jiang, Z. Yang, P. Hu and Y. H. Huang, *Chem. Eur. J.*, 2014, **20**, 1383-1388.
30. V. Etacheri, J. E. Yourey and B. M. Bartlett, *ACS Nano*, 2014, **8**, 1491-1499.
31. L. T. Anh, A. K. Rai, T. V. Thi, J. Gim, S. Kim, E.-C. Shin, J.-S. Lee and J. Kim, *J. Power Sources*, 2013, **243**, 891-898.
32. H. Usui, S. Yoshioka, K. Wasada, M. Shimizu and H. Sakaguchi, *ACS Appl. Mater. Interfaces.*, 2015, **7**, 6567-6573.
33. J. Brumbarov, J. P. Vivek, S. Leonardi, C. Valero-Vidal, E. Portenkirchner and J. Kunze-Liebhauser, *J. Mater. Chem. A*, 2015, **3**, 16469-16477.
34. K. Shen, H. Chen, F. Klaver, F. M. Mulder and M. Wagemaker, *Chem. Mater.*, 2014, **26**, 1608-1615.
35. J. Jamnik and J. Maier, *Phys. Chem. Chem. Phys.*, 2003, **5**, 5215-5220.
36. J. Maier, *Nat. Mater.*, 2005, **4**, 805-815.
37. G. Kresse and J. Hafner, *Phys. Rev. B*, 1994, **49**, 14251-14269.
38. G. Kresse and D. Joubert, *Phys. Rev. B*, 1999, **59**, 1758-1775.
39. J. P. Perdew, K. Burke and M. Ernzerhof, *Phys. Rev. Lett.*, 1996, **77**, 3865-3868.
40. H. J. Monkhorst and J. D. Pack, *Phys. Rev. B*, 1976, **13**, 5188-5192.
41. D. V. Bavykin, J. M. Friedrich and F. C. Walsh, *Adv. Mater.*, 2006, **18**, 2807-2824.
42. T. Beuvier, M. Richard-Plouet and L. Brohan, *J. Phys. Chem. C*, 2009, **113**, 13703-13706.
43. J. G. Yu, Q. Li, S. W. Liu and M. Jaroniec, *Chem. Eur. J.*, 2013, **19**, 2433-2441.
44. J. Wang, D. N. Tafen, J. P. Lewis, Z. L. Hong, A. Manivannan, M. J. Zhi, M. Li and N. Q. Wu, *J. Am. Chem. Soc.*, 2009, **131**, 12290-12297.
45. T. Okato, T. Sakano and M. Obara, *Phys. Rev. B*, 2005, **72**, 115124.

-
46. H. Y. Chen, A. Nambu, W. Wen, J. Graciani, Z. Zhong, J. C. Hanson,
E. Fujita and J. A. Rodriguez, *J. Phys. Chem. C*, 2006, **111**, 1366-
1372.
47. A. Fujishima, X. T. Zhang and D. A. Tryk, *Sur. Sci. Rep.*, 2008, **63**,
5 515-582.
48. Y. M. Wu, M. Y. Xing, J. L. Zhang and F. Chen, *Appl. Catal. B: Environ.*, 2010, **97**, 182-189.
49. L. F. Shen, X. G. Zhang, H. S. Li, C. Z. Yuan and G. Z. Cao, *J. Phys. Chem. Lett.*, 2011, **2**, 3096-3101.
- 10 50. J. S. Chen, Y. L. Tan, C. M. Li, Y. L. Cheah, D. Y. Luan, S. Madhavi,
F. Y. C. Boey, L. A. Archer and X. W. Lou, *J. Am. Chem. Soc.*, 2010,
132, 6124-6130.
51. K. Shin, H. J. Kim, J. M. Choi, Y. M. Choi, M. S. Song and J. H. Park,
Chem. Commun., 2013, **49**, 2326-2328.
- 15 52. J. Y. Shin, D. Samuelis and J. Maier, *Adv. Funct. Mater.*, 2011, **21**,
3464-3472.
53. M. Zúcalov, M. Kalbac, L. Kavan, I. Exnar and M. Graetzel, *Chem. Mater.*, 2005, **17**, 1248-1255.
54. P. Balaya, A. J. Bhattacharyya, J. Jamnik, Y. F. Zhukovskii, E. A.
20 Kotomin and J. Maier, *J. Power Sources*, 2006, **159**, 171-178.
55. K. M. Shaju, G. V. S. Rao and B. V. R. Chowdari, *J. Electrochem. Soc.*, 2003, **150**, A1-A13.

For table of contents entry



Unique TiO₂ nanotube assemblies with tailored architectures and crystal phases are fabricated for lithium-storage applications.